Supplemental information

Probing the core and surface composition of nanoalloy to rationalize its selectivity: Study of Ni-Fe/SiO$_2$ catalysts for liquid-phase hydrogenation

Dichao Shi, Achraf Sadier, Jean-Sébastien Girardon, Anne-Sophie Mamede, Carmen Ciotonea, Maya Marinova, Lorenzo Stievano, Moulay T. Sougrati, Camille La Fontaine, Sébastien Paul, Robert Wojcieszak, and Eric Marceau

Supplemental Experimental Procedures:

Catalyst characterization

Powder X-ray diffraction patterns (XRD) were recorded in ambient conditions using the Cu Kα radiation (λ = 1.5418 Å; 40 kV, 30 mA) on a Siemens D5000 diffractometer, with a 0.05° scan step and 2 s time step. X-ray fluorescence spectroscopy (XRF; M4 Tornado, Bruker) was used to estimate the elemental composition of the reduced catalysts. To obtain accurate quantification of the metals loading in the catalysts, each sample was irradiated 30 times. Fe and Ni elemental analysis was also performed on dried solids by inductively coupled plasma-optic emission spectroscopy, using a 720-ES ICP-OES spectrometer (Agilent) with axial viewing and simultaneous CCD detection. N_2 physisorption isotherms at liquid nitrogen temperature were carried out on a TriStar II Plus gas adsorption analyzer (Micromeritics) after activation at 150 °C in vacuum overnight. The specific surface area was evaluated with the Brunauer-Emmett-Teller (BET) model over the range P/P_0 = 0.05 – 0.30. Temperature-programmed reduction (TPR) was followed using an Autochem apparatus (Micromeritics) under H_2 (5 %)/Ar (flow rate: 50 mL min^{-1}; ramp rate: 7.5 °C min^{-1}).

Electron microscopy was carried out on the microscopy facility of the Advanced Characterization Platform of the Chevreul Institute, Lille. Bright-field TEM images for the determination of size histograms were obtained using a Tecnai G2 20 microscope equipped with a LaB$_6$ filament and operating at 200 kV. Between 100 and 200 particles were counted in each case. For the analysis of individual nanoparticles, high resolution Scanning Transmission Electron Microscopy (STEM) was performed on a TITAN Themis 300 S/TEM microscope equipped with: a probe aberration corrector and monochromator, allowing spatial resolution of 70 pm and energy resolution of 150 meV; a super-X windowless 4 quadrant SDD (silicon drift detector) detection system for STEM-EDX mapping and several annual dark field detectors; a high resolution post-column GIF, the GATAN's Quantum ERS/966 with 2kx2k Ultrascan camera with 994G sensor, for the acquisition of electron energy loss spectra. In order to investigate the elemental distribution within bimetallic particles, high-angle annular dark field (HAADF) imaging and high-resolution electron energy loss spectroscopy (HR-EELS) were carried out in the STEM mode. Measurements were performed with a spot size of about 500 pm, a semi-convergence angle between 16 and 21 mrad, and a probe current of approximately 100 pA. For HAADF images, collection angles were chosen between 50 and 200 mrad. Dual EELS acquisition was performed in the spectral imaging mode with a collection angle of 49 mrad, a dispersion of 0.25 eV/ch, a step between 150 and 700 pm, and a dwell time between 50 and 200 ms. Alignment of the energy drift was done on the zero-loss peak. When possible, noise reduction by PCA was performed on the spectrum images using HyperSpy.

Catalytic tests and recycling

The hydrogenation of furfural was tested using a Screening Pressure Reactor (SPR) system from Unchained Labs equipped with 24 parallel stainless-steel batch reactors of 6 mL each. Tests were performed at 150 °C under 20 bar H_2 and a continuous agitation of 600 rpm for all the tests (orbital shaking). Catalysts formerly reduced at 700 °C and stored in air were weighed, introduced into the reactors, and re-activated *in situ* at 400 °C in pure H_2 for 2 h (400 °C being the highest temperature that can be attained in the set-up). 1.5 mL of FF solution in isopropanol was then added into each reactor inside a glove-box, in order to avoid the re-oxidation of the catalysts. All the solutions tested by GC after reaction were filtered to eliminate the catalyst. Reaction products were analyzed using a Shimadzu GC-2010 Plus gas chromatograph, equipped with a FID detector, a ZB-5MS column (30 m x 0.25 mm x 0.25 μm).

The amount of furfural was fixed at 0.56 mmol (concentration: 0.37 mol L^{-1}), in order to minimize the amounts of ethers formed between the alcohols resulting from the hydroconversion of FF and the isopropanol solvent.[23] A mass of 10 mg of catalyst was first used for different reaction times, 1, 2 and 4 h. However, it was found that for the most active catalysts, conversion already reached 100 % for the shortest reaction time, which did not allow comparison with the less active systems, or estimation of an initial reaction rate. A significant decrease of the conversion could only be achieved by decreasing both the reaction time and the catalyst mass at the same time, while staying in satisfactory accuracy domains. The following couples of parameters were thus used: 0.5 h, 3 mg; 0.5 h, 5 mg; 1 h, 3 mg; 1 h, 5 mg. As a consequence, the catalysis figures will be plotted as a function of the product between reaction time and the mass of catalyst, namely: 1.5 (0.5 h * 3 mg), 2.5 (0.5 h * 5 mg), 5 (1 h * 5 mg), 10 (1 h * 10 mg), 20 (2 h * 10 mg) and 40 h * mg (4 h * 10 mg). As selectivities cannot be compared at identical conversion across the whole catalysts series, given the very different catalytic performance, furfural consumption and yields of products will be compared, using mmol as unit. The slope of the curves will thus correspond to reaction rates expressed in mmol of FF consumed per mg of catalyst and per hour (mmol mg$_{cat}^{-1}$ h^{-1}), which will be further normalized per m^2 of exposed metal.

In order to evaluate the stability of the Ni$_{62}$Fe$_{38}$/SiO$_2$ and Ni$_{100}$/SiO$_2$ catalysts, recycling experiments were conducted in a batch Parr reactor, employing a larger mass of catalyst (**Table S12**). A reaction time of 65 min and 35 min, respectively, was selected in order to detect the production of secondary and tertiary products, while keeping the conversion under 100 %. After the first run, the catalyst was collected by centrifugation, washed with isopropanol, and dried at 60 °C overnight. The catalyst was re-activated under a flow of H_2 at 400 °C for 2 h before each run.

The carbon balance was higher than 90 % during the recyclability tests. In the first run, selectivities were found to be in the same ranges as those measured using the SPR set-up at close conversion (for instance, for $Ni_{62}Fe_{38}/SiO_2$, conversion of 91% for (time * mass) = 10 h mg : FFA, 83.9%, iPrOMF, 7.4%, THFFA, 3.3%, MF, 5.4%; for Ni_{100}/SiO_2 at a conversion of 76%, (time * mass) = 5 h mg : FFA, 30.0%, iPrOMF, 34.1%, THFFA, 11.3%, MF, 18.9%, MTHF, 5.8%). The production of secondary products was less marked in the Parr reactor. It should be remembered that the geometry of the reactors, their volume, and the mode of stirring are noticeably different. However, the high selectivity of $Ni_{62}Fe_{38}/SiO_2$ to FFA, and the rise of the secondary pathways for Ni_{100}/SiO_2, were clearly confirmed.

The catalytic activity remained high for three runs of reaction for the two catalysts, though it was seen to drop during the third run. Upon recycling, the selectivity toward FFA increased, much more markedly for Ni_{100}/SiO_2, while the weight of the secondary pathways decreased. $Ni_{62}Fe_{38}/SiO_2$ still remained the more selective to FFA of the two.

It was verified by XRF on the catalysts recovered after three runs of reaction that no major leaching of Ni or Fe could be evidenced (the use of an organic solvent precluded the search by ICP of traces of metals in the solutions). TEM measurements showed that a population of particles larger than 7 nm was now detected, which may account for the lower conversion measured during the third run (**Figure S12**). A similar coalescence of the particles was observed when the catalysts were used for the aqueous-phase hydrogenation of xylose to xylitol,[15] but, in contrast with this reaction in water, the Ni catalyst here was not transformed back to its initial phyllosilicate form. Moreover, the decrease of the selectivity to iPrOMF for the two catalysts suggests that more Ni^{2+} sites became reduced after each activation step (see the discussion about the sites catalyzing the etherification reactions). Finally, the surface Ni and Fe molar proportions, measured by LEIS on recycled $Ni_{62}Fe_{38}/SiO_2$, did not change significantly (**Figure S13**).

EXAFS fits for the Ni-Fe/SiO₂ catalysts after re-activation in H₂ at 500 °C

Three compositions were tested for the fit of the first shell at the Ni K-edge: nickel atoms only; iron atoms only; nickel and iron atoms. The latter hypothesis was discarded for the three Ni-richer catalysts, as the fit led to a negative number of Fe atoms. Besides, the goodness of the fit was always lower when using a set of Fe atoms than when using a set of Ni atoms. **Tables S5** and **S6** show different hypotheses for the fits of $Ni_{35}Fe_{65}/SiO_2$ and $Ni_{55}Fe_{45}/SiO_2$, the two catalysts with the highest iron loadings. The Fe model was rejected for $Ni_{55}Fe_{45}/SiO_2$ on the basis of a poor value of χ^2. For both $Ni_{35}Fe_{65}/SiO_2$ and $Ni_{55}Fe_{45}/SiO_2$, combining Ni and Fe atoms in the first shell led to an acceptable total number of neighbors (lower than 12 as expected in a bulk *fcc* environment) but also to high uncertainties in the assessment of the interatomic distances and of the Debye-Waller factors. These uncertainties remained high when assigning the same Debye-Waller factor to the two types of atoms. Moreover, the Ni-Fe distance was found in both cases to be slightly shorter than the Ni-Ni distance, which is at odds with the relative size of the two atoms. It was thus chosen to model the first shell of the five catalysts with Ni atoms only. The values of N found for $Ni_{35}Fe_{65}/SiO_2$ and $Ni_{55}Fe_{45}/SiO_2$, larger than 12 and correlated to high values of σ^2 (**Table S7**), nevertheless indicate that for these two catalysts, modelling the first shell with Ni atoms only is certainly simplistic.

At the Fe K-edge (**Table S8**), fits were always improved when adding an oxidic contribution to the metallic shell of nearest neighbors, and uncertainties decreased when assigning the same Debye-Waller factor to the two shells. The distance between Fe and O (1.95 – 1.97 Å) is characteristic of Fe(III) ions in an oxidic phase. Adding oxidized Fe^{3+} in a shell at a longer distance, as would become to an Fe-rich oxide like hematite, resulted in a satisfactory fit, but with a low contribution from the oxidic phase. Despite this small contribution, EXAFS signals were dominated by the response of metallic Fe. Finally, a feature already noticed at the Ni edge is the joint drift of N(Ni) and σ^2 towards higher values when the proportion of Fe increases (**Table S8**), a sign that modelling the first shell with one type of metal only is probably a strong approximation for Fe-rich systems.

Temperature-programmed reduction (H2-TPR)

The reducibility of the Ni-Fe/SiO2 systems were recorded by temperature-programmed reduction after drying at 60 °C to eliminate adsorbed water. Globally speaking, the three main reduction stages can be interpreted by comparison with the process evidenced by X-ray absorption and Mössbauer spectroscopy for Ni62Fe38/SiO2.[14] The peak below 400 °C is linked to the onset of the reduction of Fe3+ to Fe2+. Its intensity accordingly decreases when the Fe content decreases. The major composite peak at 400 – 500 °C includes the total reduction of Ni2+ to metallic Ni and initiation of the reduction of Fe2+ to metallic Fe. The last stage between 500 and 700 °C would correspond to the completion of the reduction of Fe. However, this interpretation does not hold for Ni84Fe16/SiO2, Ni92Fe8/SiO2 and Ni100/SiO2, as the peak between 550 and 750 °C becomes more intense and shifts to higher temperature with increasing Ni content, and not with increasing Fe content. We suggest to correlate this kinetic delay with a higher degree of organization of the phyllosilicate phase formed by DPU when moving to the monometallic system, compared with mixed systems in which ions bearing different charges, Ni2+ and Fe3+, have to co-exist in significant amounts. The evolution of the specific surface area supports this hypothesis.

Mössbauer spectroscopy

The Mössbauer spectra of the dried materials were asymmetric and be fitted with two different quadrupole split contributions and slightly different isomer shifts, as is usually done for the sake of simplicity, for ions present in a continuum of slightly variating environments. The relatively low isomer shift of the narrower, major doublet (orange curves on **Figure S16**) is similar to that of octahedrally coordinated Fe^{3+} in mixed Ni-Fe ferrites. The significant decrease of the average quadrupole splitting with the Ni content is evidenced in the scheme to the right of this paragraph. The quadrupole splitting of the wider, minor doublet (blue curves) is noticeably larger than the values typically observed for bulk iron oxyhydroxides and silicates. This can be related to distortions of the chemical environment around Fe^{3+}.[14] The decrease of the average quadrupole splitting can thus be linked to a lower degree of structural and chemical heterogeneities around Fe^{3+}, as the existence of a mixed Fe^{3+} / Ni^{2+} environment around Fe^{3+} becomes less likely when the Ni content increases.
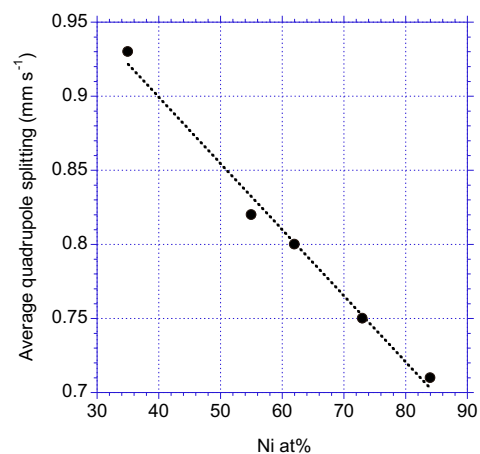
Table S1. Representative catalysts and experimental conditions favouring the hydrogenation of furfural for nickel and nickel based catalysts.

| No.	Catalyst	Reaction conditions	Conv.(%)	Y_{FFA}(%)	REF
1	Ni-Ce-B	180°C, 10bar H_2, 3h, 30mL ethanol	96.8	N.D.	[1]
2	Ni-Fe-B	200°C, 10bar H_2, 4h, 30mL ethanol	100	~100	[2]
3	$Cu_{11.2}Ni_{2.4}$-MgAlO	300°C, 10bar H_2, 90mL ethanol	89.9	87.0	[3]
4	MoNiB/γ-Al_2O_3	80°C, 50bar, 3h, methanol solvent	99.1	90.2	[4]
5	$Ni_{74.5}P_{12.1}B_{13.4}$	250psi, 80°C, furfural/ethanol=2mL/170mL	~95	~77.9	[5]
6	2wt% Ni/SiO_2	100°C, 10MPa H_2, 8h, 50mL propanol-2-ol solvent	31	23.6	[6]
7	Cu-Fe	160°C, 90bar H_2, 5h	91.0	89.5	[7]
8	Raney Ni-CuPMo12	80°C, 20bar H_2, 1h, ethanol solvent	98	97	[8]
9	Ni-Ce-B alloy	80°C, 10bar H_2, 3h, ethanol solvent	97	~97	[2]
10	Ni-Sn	110°C, 30bar H_2, 1.25h, isopropanol solvent	72	70	[9]
11	Ni-Sn/TiO_2	110°C, 30bar H_2, 1.25h, isopropanol solvent	>99	>99	[9]
12	7.0wt%, $Fe_{29}Ni_{71}$/SiO_2	250°C, H_2/Furfural=25, P=1bar, W/F = 0.1h (phase gaz)	98	10	[10]
13	18 wt%, $Fe_{42}Ni_{58}$/Carbon	150°C, 10bar H_2, WHSV=60h^{-1}, ethanol solvent	99	90	[11]
14	20 wt%, $Fe_{25}Ni_{75}$/Al_2O_3	150 °C, 30bar H_2, isopropanol solvent	95	97	[12]
15	$Fe_{36.0}Ni_{34.1}B_{29.9}$	100°C, 10bar H_2, ethanol solvent	~100	~100	[2]
16	$Fe_{40.44}$ $Ni_{0.51}$-$O_{40.94}Si_{18.11}$	250 °C, 20 bar H_2, $W_{Catalyst}$=60mg	94	~100	[14]
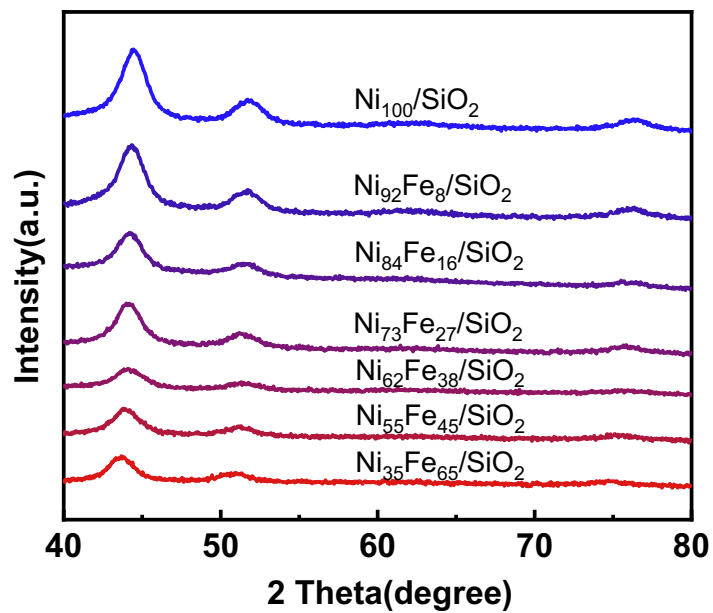
Figure S1. XRD patterns recorded on reduced catalysts.

Table S2. Unit cell parameter calculated for Ni-Fe bimetallic particles after reduction at 700 °C and exposure to air, assessed from a linear Vegard correlation.[1]

Samples	a (nm)
$Ni_{35}Fe_{65}/SiO_2$	0.3593
$Ni_{55}Fe_{45}/SiO_2$	0.3572
$Ni_{62}Fe_{38}/SiO_2$	0.3563
$Ni_{73}Fe_{27}/SiO_2$	0.3554
$Ni_{84}Fe_{16}/SiO_2$	0.3541
$Ni_{92}Fe_8/SiO_2$	0.3535
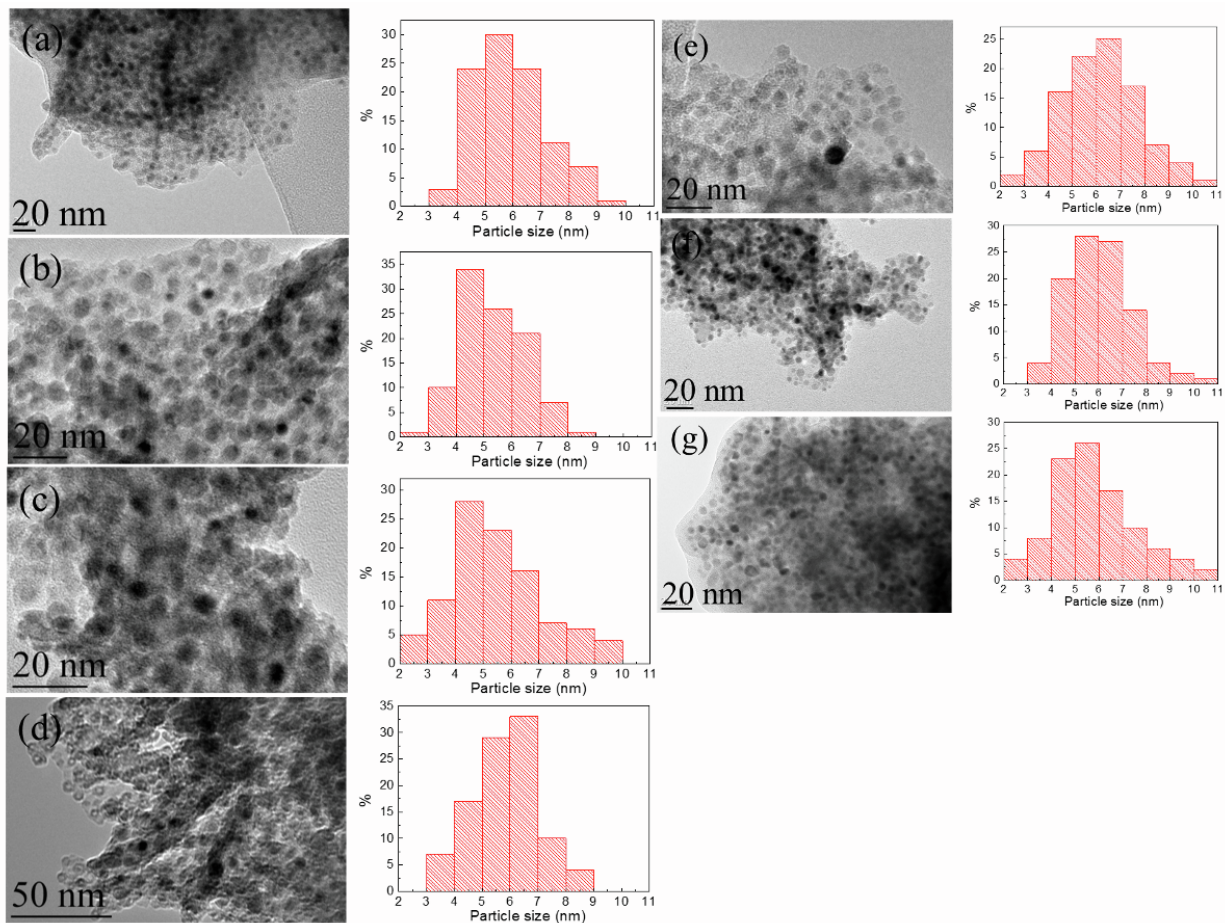
Figure S2. Bright field TEM micrographs and particle size distributions measured by TEM for $Ni_{35}Fe_{65}/SiO_2$ (a), $Ni_{55}Fe_{45}/SiO_2$ (b), $Ni_{62}Fe_{38}/SiO_2$ (c), $Ni_{73}Fe_{27}/SiO_2$ (d), $Ni_{84}Fe_{16}/SiO_2$ (e), $Ni_{92}Fe_8/SiO_2$ (f) and Ni_{100}/SiO_2 (g) after reduction at 700 °C and exposure to air.

Table S3. Average particle size, evaluated from X-ray diffraction (Scherrer equation) and from TEM size histograms, metal dispersion and specific surface area of exposed metal, for bimetallic Ni-Fe/SiO₂ catalysts and monometallic Ni/SiO₂ catalyst reduced at 700 °C.

Samples	Average particle size (nm)		Dispersion (%)	Metal surface area (m^2 g_{cat}^{-1})
	XRD	TEM		
$Ni_{35}Fe_{65}/SiO_2$	6	5.4 (0.5)[a]	17	72.6
$Ni_{55}Fe_{45}/SiO_2$	6	4.8 (0.9)	19	63.1
$Ni_{62}Fe_{38}/SiO_2$	5	5.0 (0.8)	19	63.1
$Ni_{73}Fe_{27}/SiO_2$	5	5.3 (0.5)	17	62.2
$Ni_{84}Fe_{16}/SiO_2$	6	5.7 (0.6)	17	63.3
$Ni_{92}Fe_{8}/SiO_2$	5	5.5 (0.4)	17	66.8
Ni_{100}/SiO_2	5	5.3 (0.7)	18	71.9

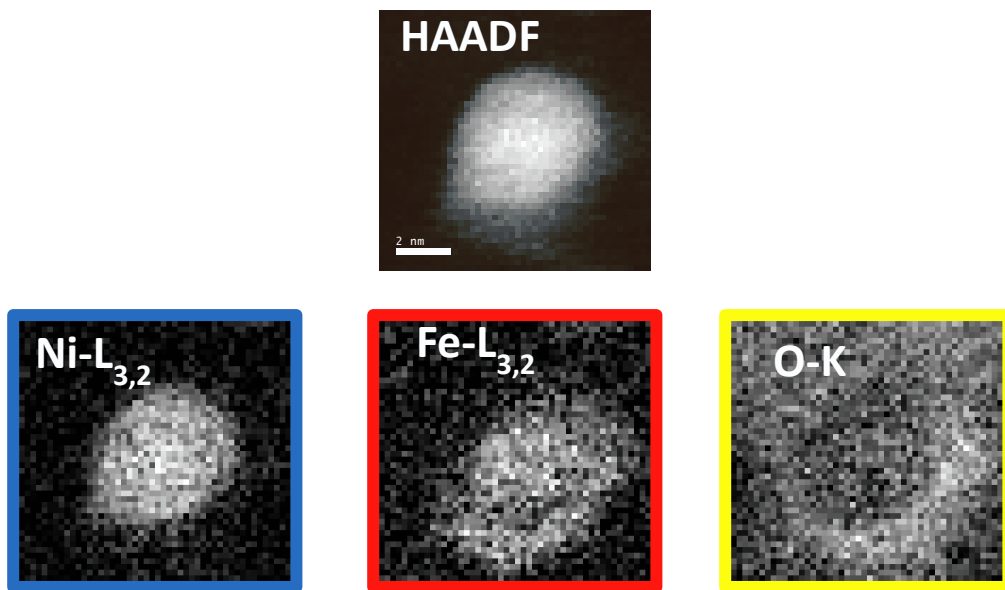[a] In brackets: standard deviation

Figure S3. STEM - HAADF image of the particle singled out on Figure 1b1-2 (catalyst $Ni_{62}Fe_{38}/SiO_2$), and composition maps for Ni-L$_{3,2}$ edge at 856.5 eV, Fe-L$_{3,2}$ edge at 710.5 eV and O-K edge at 531.0 eV, obtained by STEM - EELS mapping. Increasing brightness indicates a larger proportion of the element.

Table S4. Molar proportions extracted from STEM - EELS mapping of the core of individual particles reduced at 700 °C and exposed to air.

Samples	$Ni_{55}Fe_{45}/SiO_2$		$Ni_{62}Fe_{38}/SiO_2$ *		$Ni_{73}Fe_{27}/SiO_2$		$Ni_{84}Fe_{16}/SiO_2$	
	Ni %	Fe %	Ni %	Fe %	Ni %	Fe %	Ni %	Fe %
	40	60	79	21	79	21	94	6
	51	49	69	31	70	30	85	15
	45	55	69	31	76	24	90	10
	58	42	40	60	75	25	85	15
	60	40	70	30	81	19	90	10
	58	42	62	38	73	27	87	13
	51	49	67	33	70	30	86	14
	42	58	60	40	69	31	87	13
	55	45	54	46	74	26	82	18
	60	40			73	27		
Average	52	48	63	37	74	26	88	12
Standard deviation		7%		10%		4%		3%
XRD (Tab. 1)	55	45	63	37	71	29	84	16

Standard deviation for Fe: 7 at%

* Measurements carried out on 28 particles from a similar sample in Shi *et al.*,[14] led to metal proportions of 69 % for Ni and 31 % for Fe, and a standard deviation of 8 at% of Fe.
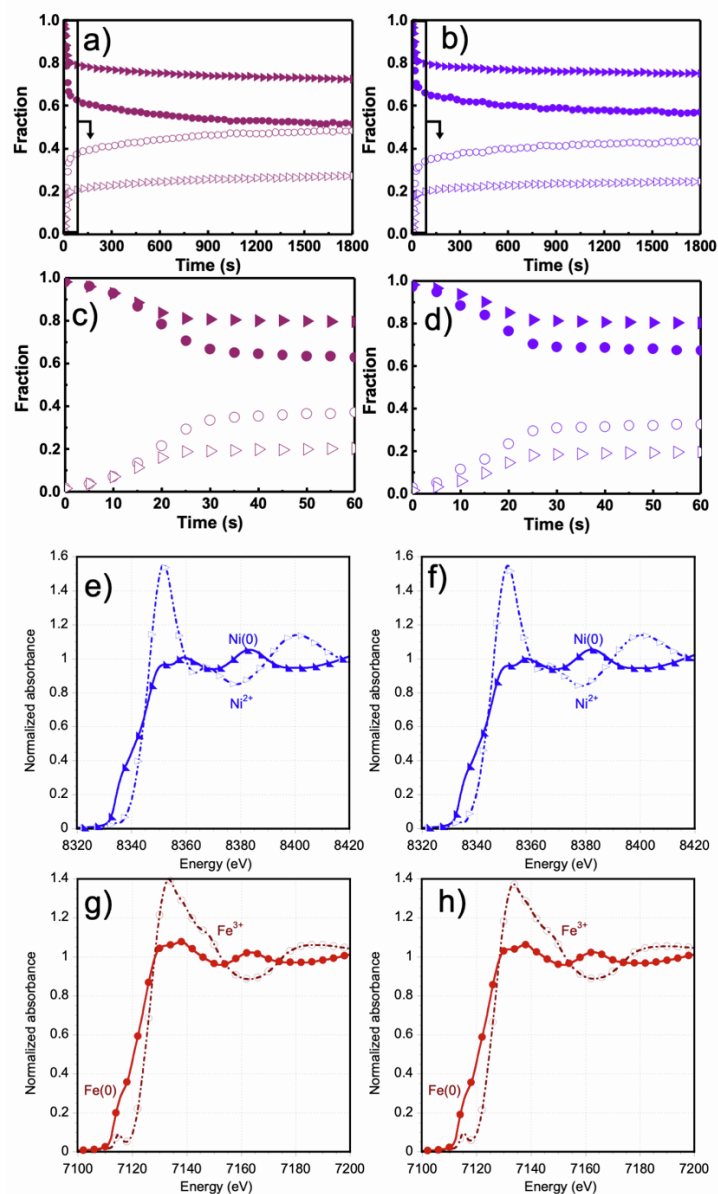
Figure S4. X-ray absorption spectroscopy: Figures a-d represent MCR-ALS analysis of the oxidation of reduced $Ni_{62}Fe_{38}/SiO_2$ (a) and $Ni_{84}Fe_{16}/SiO_2$ (b) catalysts under dilute O_2 at 80 °C. Full circle: reduced Fe; Blank circle: oxidized Fe; Full triangle: reduced Ni; Blank triangle: oxidized Ni. Zooms on the first minute of oxidation are presented in the figures c and d. Figure e-h represent spectral components extracted via the MCR-ALS procedure for the oxidation of $Ni_{62}Fe_{38}/SiO_2$ (e and g) and $Ni_{84}Fe_{16}/SiO_2$ (f and h); Figures e and f: Ni K-edge, figures g and h: Fe K-edge. Symbols shown correspond to every 10th scanned energy.
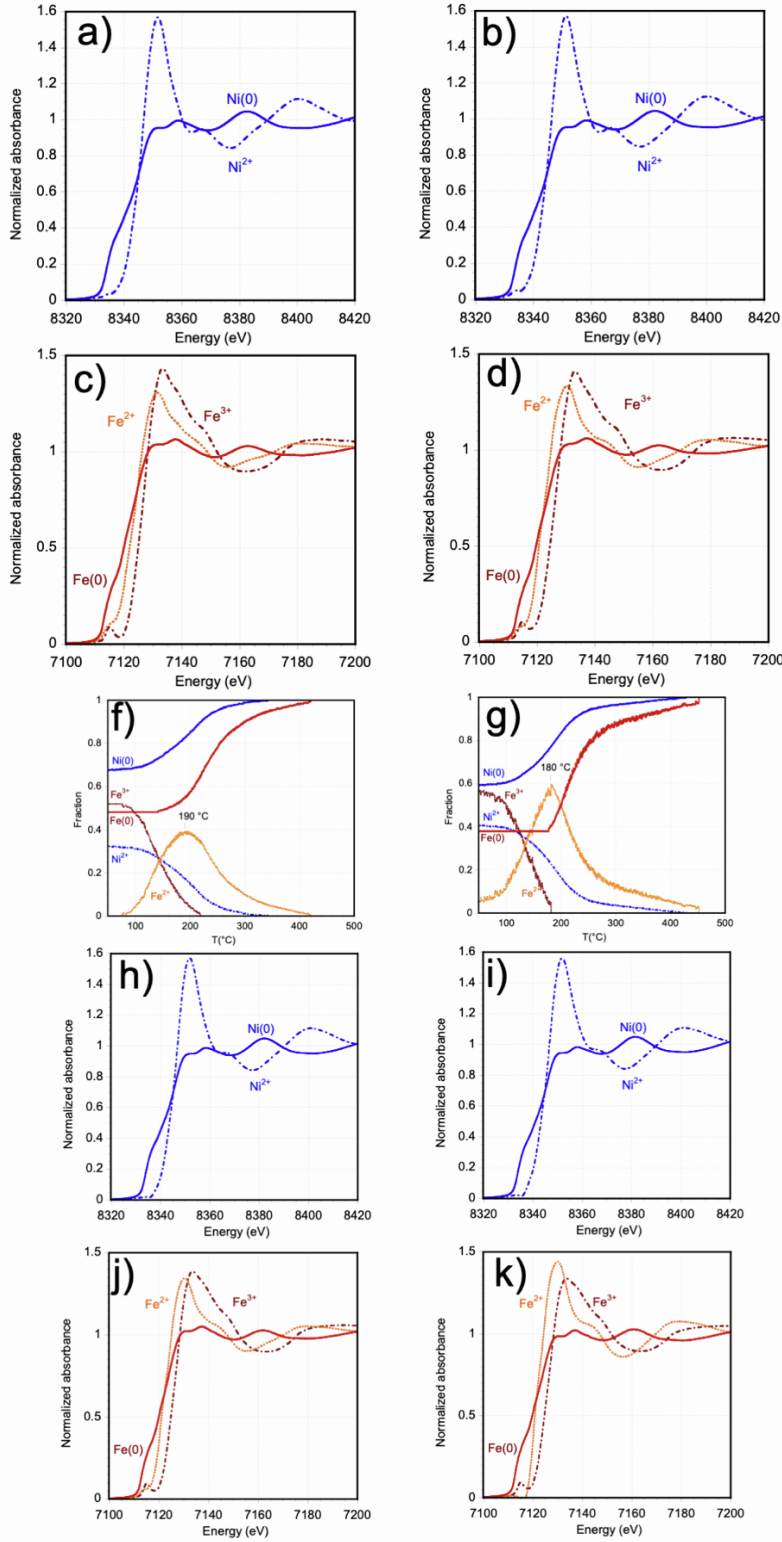
Figure S5. X-ray absorption spectroscopy: concentration profiles obtained from MCR-ALS analysis of the activation under H_2 of (a and c) $Ni_{55}Fe_{45}/SiO_2$, (b and d) $Ni_{62}Fe_{38}/SiO_2$; (f, h, j) $Ni_{73}Fe_{27}/SiO_2$ and (g, I, k) $Ni_{84}Fe_{16}/SiO_2$; corresponding spectral components at the Ni K-edge (h, i) and Fe K-edge (j, k).
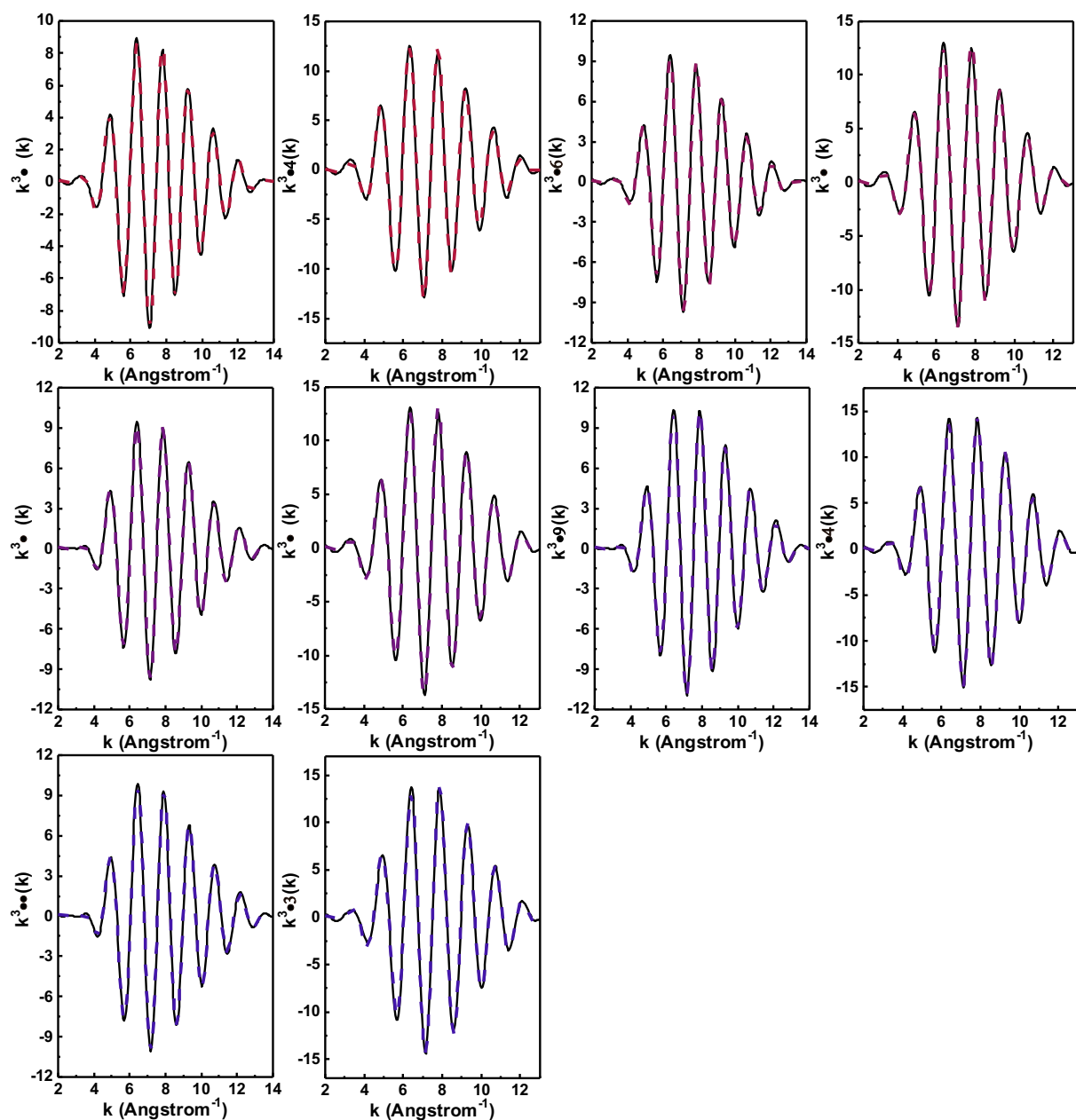
Figure S6. EXAFS k^3-weighted oscillations and results of $k^3 \chi$ (k) EXAFS fitting of the first shell in k-space after temperature-programmed reduction: $Ni_{35}Fe_{65}/SiO_2$ (a1 and a2), $Ni_{55}Fe_{45}/SiO_2$ (b1 and b2), $Ni_{62}Fe_{38}/SiO_2$ (c1 and c2), $Ni_{73}Fe_{27}/SiO_2$ (d1 and d2) and $Ni_{84}Fe_{16}/SiO_2$ (e1 and e2) at the Fe K-edge and Ni K-edge (black: experimental; colored: fit; spectra recorded at 80°C after a ramp in H_2 to 500 °C).

Figure S7. EXAFS k^3-weighted Fourier transform moduli and results of $k^3 \chi$ (k) EXAFS fitting for the first shell in R-space:

$Ni_{35}Fe_{65}/SiO_2$ (a1 and a2), $Ni_{55}Fe_{45}/SiO_2$ (b1 and b2), $Ni_{62}Fe_{38}/SiO_2$ (c1 and c2), $Ni_{73}Fe_{27}/SiO_2$ (d1 and d2) and $Ni_{84}Fe_{16}/SiO_2$

(e1 and e2) at the Fe K-edge and Ni K-edge (black: experimental; colored: fit; spectrum recorded at 80°C after a ramp in
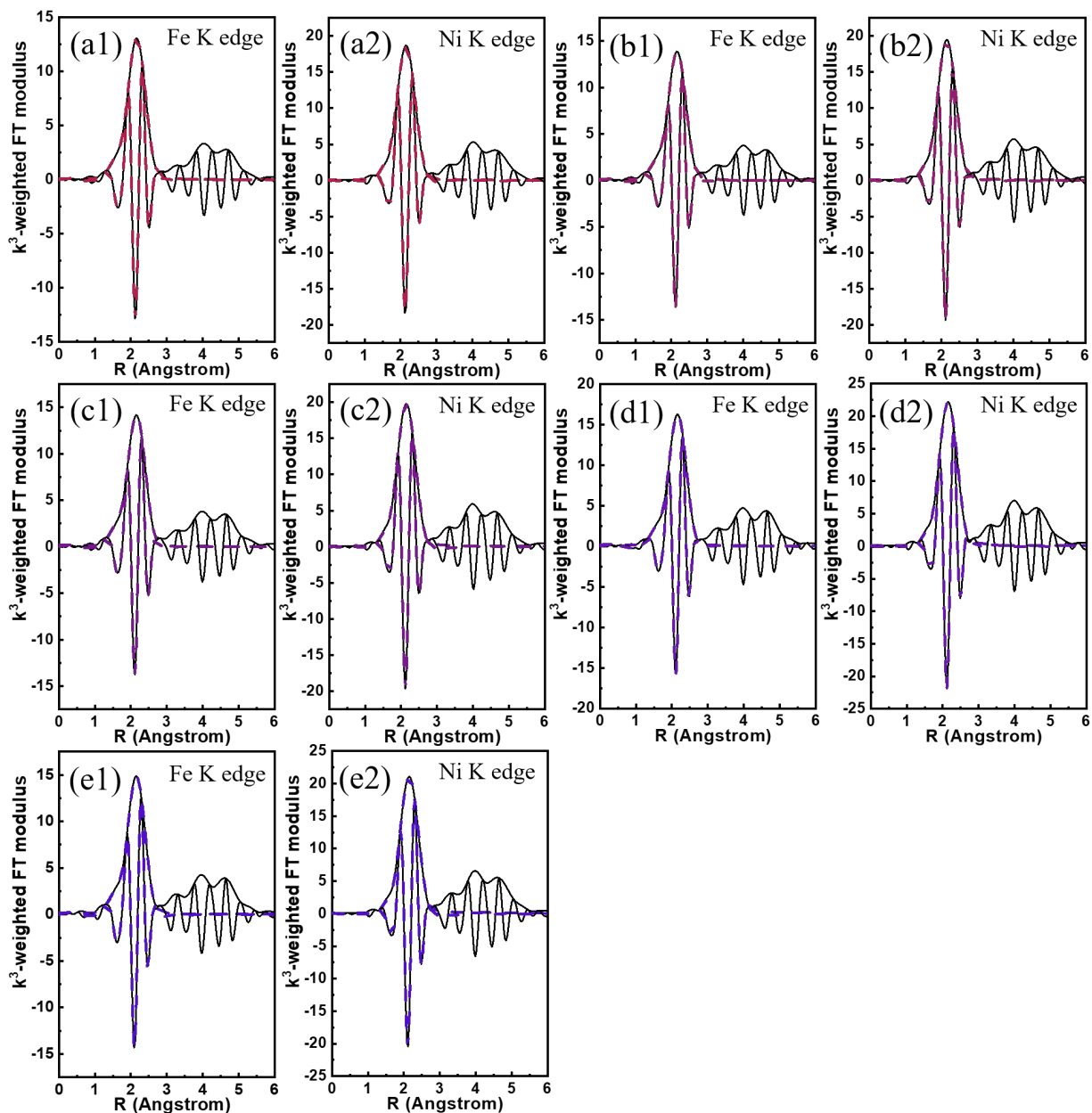
H_2 to 500 °C). Interatomic distances R are listed in **Table S5**.

Table S5. Fitted parameters at the Ni K-edge for sample $Ni_{35}Fe_{65}/SiO_2$: influence of the choice of nearest neighbors on the fit goodness and uncertainties.

Backscatterer	N	σ^2 (Å^2) x 10^3	R (Å)
Ni	12.9 ± 0.8	10.1 ± 0.5	2.512 ± 0.004
r-factor = 0.00216, χ^2 = 433, N_{ind} = 10, N_{var} = 4			
Fe	9.2 ± 0.6	7.4 ± 0.6	2.524 ± 0.004
r-factor = 0.00308, χ^2 = 620, N_{ind} = 10, N_{var} = 4			
Ni	7.5 ± 4.0	8 ± 5	2.54 ± 0.04
Fe	3.6 ± 2.7	6 ± 5	2.47 ± 0.07
r-factor = 0.00140, χ^2 = 528, N_{ind} = 10, N_{var} = 7			
Ni	8.2 ± 4.6	9 ± 2	2.52 ± 0.02
Fe	3.3 ± 3.3	9 ± 2	2.5 ± 0.1
r-factor = 0.00151, χ^2 = 436, N_{ind} = 10, N_{var} = 6			

Table S6. Fitted parameters at the Ni K-edge for sample $Ni_{55}Fe_{45}/SiO_2$: influence of the choice of nearest neighbors on the fit goodness and uncertainties.

Backscatterer	N	σ^2 (Å^2) x 10^3	R (Å)
Ni	12.3 ± 0.6	9.4 ± 0.5	2.504 ± 0.004
	r-factor = 0.00183, χ^2 = 665, N_{ind} = 10, N_{var} = 4		
Fe	8.8 ± 0.6	6.7 ± 0.7	2.516 ± 0.005
	r-factor = 0.00455, χ^2 = 1609, N_{ind} = 10, N_{var} = 4		
Ni	9.2 ± 4.2	8 ± 4	2.52 ± 0.03
Fe	2.0 ± 2.7	5 ± 7	2.44 ± 0.09
	r-factor = 0.00140, χ^2 = 528, N_{ind} = 10, N_{var} = 7		
Ni	10.2 ± 5.1	9 ± 2	2.51 ± 0.01
Fe	1.5 ± 3.5	9 ± 2	2.5 ± 0.2
	r-factor = 0.00166, χ^2 = 865, N_{ind} = 10, N_{var} = 6		

Table S7. Fitted parameters at the Ni K-edge ($E_0 = 8340 \pm 1.4$ eV, $S_0^2 = 0.77$) and Fe-K edge ($E_0 = 7720.0 \pm 1.5$ eV, $S_0^2 = 0.76$) determined from the EXAFS analysis of the spectra recorded at 80 °C for the Ni-Fe/SiO$_2$ catalysts after a ramp in H$_2$ at 500 °C.

	Ni K-edge				Fe K-edge			
	Back scatterer	N	σ^2 (Å^2) x 10^3	R (Å)	Back scatterer	N	σ^2 (Å^2) x 10^3	R (Å)
Ni$_{35}$Fe$_{65}$/					O	0.5 ± 0.3	10.0 ± 0.7	1.95 ± 0.04
SiO$_2$	Ni	12.9 ± 0.8	10.1 ± 0.5	2.512 ± 0.004	Ni	9.0 ± 0.6	10.0 ± 0.7	2.520 ± 0.005
	r-factor = 0.00216, χ^2 = 433, N_{ind} = 10, N_{var} = 4				*r-factor = 0.00264, χ^2 = 1089, N_{ind} = 10, N_{var} = 6*			
Ni$_{55}$Fe$_{45}$/					O	0.8 ± 0.3	9.2 ± 0.7	1.97 ± 0.03
SiO$_2$	Ni	12.3 ± 0.6	9.4 ± 0.5	2.504 ± 0.004	Ni	8.5 ± 0.6	9.2 ± 0.7	2.511 ± 0.005
	r-factor = 0.00183, χ^2 = 665, N_{ind} = 10, N_{var} = 4				*r-factor = 0.00380, χ^2 = 1871, N_{ind} = 10, N_{var} = 6*			
Ni$_{62}$Fe$_{38}$/					O	0.9 ± 0.2	8.8 ± 0.5	1.97 ± 0.02
SiO$_2$	Ni	11.5 ± 0.6	8.8 ± 0.5	2.498 ± 0.004	Ni	8.2 ± 0.4	8.8 ± 0.5	2.505 ± 0.004
	r-factor = 0.00213, χ^2 = 543, N_{ind} = 10, N_{var} = 4				*r-factor = 0.00129, χ^2 = 747, N_{ind} = 10, N_{var} = 6*			
Ni$_{73}$Fe$_{27}$/					O	0.9 ± 0.2	8.0 ± 0.4	1.97 ± 0.02
SiO$_2$	Ni	11.3 ± 0.6	7.8 ± 0.5	2.496 ± 0.004	Ni	8.3 ± 0.4	8.0 ± 0.4	2.502 ± 0.003
	r-factor = 0.00214, χ^2 = 572, N_{ind} = 10, N_{var} = 4				*r-factor = 0.00083, χ^2 =361, N_{ind} = 10, N_{var} = 6*			
Ni$_{84}$Fe$_{16}$/					O	1.1 ± 0.2	8.4 ± 0.5	1.96 ± 0.02
SiO$_2$	Ni	10.7 ± 0.5	7.8 ± 0.4	2.491 ± 0.003	Ni	8.0 ± 0.4	8.4 ± 0.5	2.496 ± 0.004
	r-factor = 0.00256, χ^2 = 642, N_{ind} = 10, N_{var} = 4				*r-factor = 0.00129, χ^2 = 719, N_{ind} = 10, N_{var} = 6*			

Table S8. Fitted parameters at the Fe K-edge for sample $Ni_{62}Fe_{38}/SiO_2$: influence of the choice of nearest neighbors on the fit goodness and uncertainties.

Backscatterer	N	σ^2 (Å^2) x 10^3	R (Å)
Ni	8.3 ± 0.9	8.9 ± 0.9	2.490 ± 0.008
r-factor = 0.00999, χ^2 =3471, N_{ind} = 10, N_{var} = 4			
Fe	6.1 ± 0.9	6 ± 2	2.50 ± 0.01
r-factor = 0.02092, χ^2 =7248, N_{ind} = 10, N_{var} = 4			
O	1.0 ± 0.8	10 ± 14	1.96 ± 0.04
Ni	8.1 ± 0.8	8.8 ± 0.8	2.504 ± 0.006
r-factor = 0.00347, χ^2 = 2067, N_{ind} = 10, N_{var} = 7			
O	0.9 ± 0.2	8.8 ± 0.5	1.97 ± 0.02
Ni	8.2 ± 0.4	8.8 ± 0.5	2.505 ± 0.004
r-factor = 0.00129, χ^2 = 747, N_{ind} = 10, N_{var} = 6			
O	0.8 ± 0.2	8.3 ± 0.9	1.96 ± 0.03
Ni	7.4 ± 0.8	8.3 ± 0.9	2.496 ± 0.008
Fe	0.8 ± 0.6	8.3 ± 0.9	2.96 ± 0.05
r-factor = 0.00211, χ^2 = 1571, N_{ind} = 10, N_{var} = 8			

Table S9. [57]Fe Mössbauer hyperfine parameters of samples $Ni_{55}Fe_{45}/SiO_2$ and $Ni_{84}Fe_{16}/SiO_2$, after reduction at 700 ,

exposure to air and activation in H_2 at 400 °C. Spectra were recorded at 5 K.

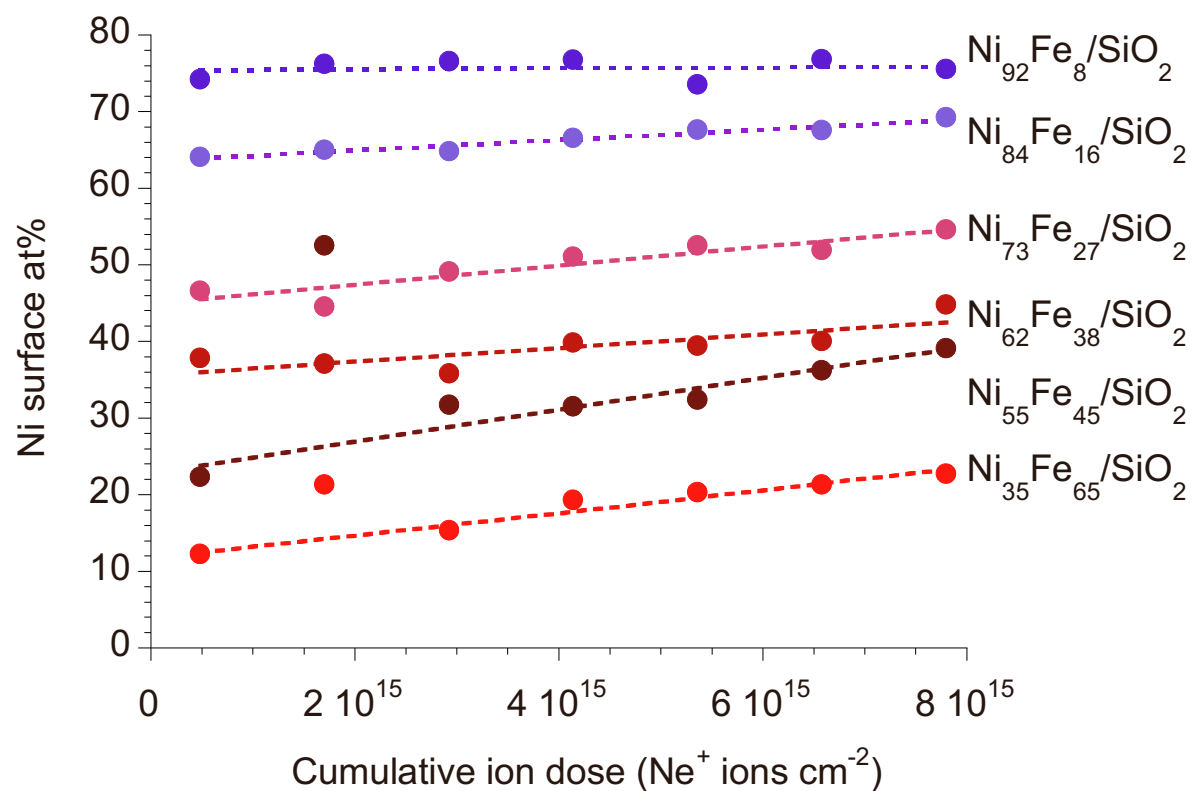| Samples	Site	δ (mm s^{-1})	Δ (mm s^{-1})	Γ (mm s^{-1})	Area (%)	B_{HF} (T)
	Fe(0), Ni-Fe core	0.15 ± 0.02	0	1.0 ± 0.1	49 ± 10	30.8 ± 0.2
$Ni_{55}Fe_{45}/SiO_2$	Fe(0), Ni-Fe surface	0.17 ± 0.03	0	1.4 ± 0.2	47 ± 10	35.5 ± 0.6
	Fe(II)	1.10 ± 0.08	1.9 ± 0.2	0.9 ± 0.2	4 ± 1	-
	Fe(0), Ni-Fe core	0.14 ± 0.02	0	1.0 ± 0.1	75 ± 5	29.0 ± 0.2
$Ni_{84}Fe_{16}/SiO_2$	Fe(0), Ni-Fe surface	0.2 ± 0.3	0	1.5 ± 0.2	16 ± 5	35.9 ± 0.9
	Fe(II)	1.1 ± 0.1	2.0 ± 0.1	1.0 ± 0.1	9 ± 2	-

Figure S8. Ni molar proportion in the outer shells determined by LEIS measurements on the six Ni-Fe catalysts, as a function of the cumulative Ne[+] ion dose. *Lines are drawn as guides for the eye only; they do not take into account measurements at 1.7 x 10^{15} ions cm^{-2} for Ni$_{35}$Fe$_{65}$/SiO$_2$ and Ni$_{55}$Fe$_{45}$/SiO$_2$, reported here for the sake of comprehensiveness but which should be considered as outliers given the general trends.*
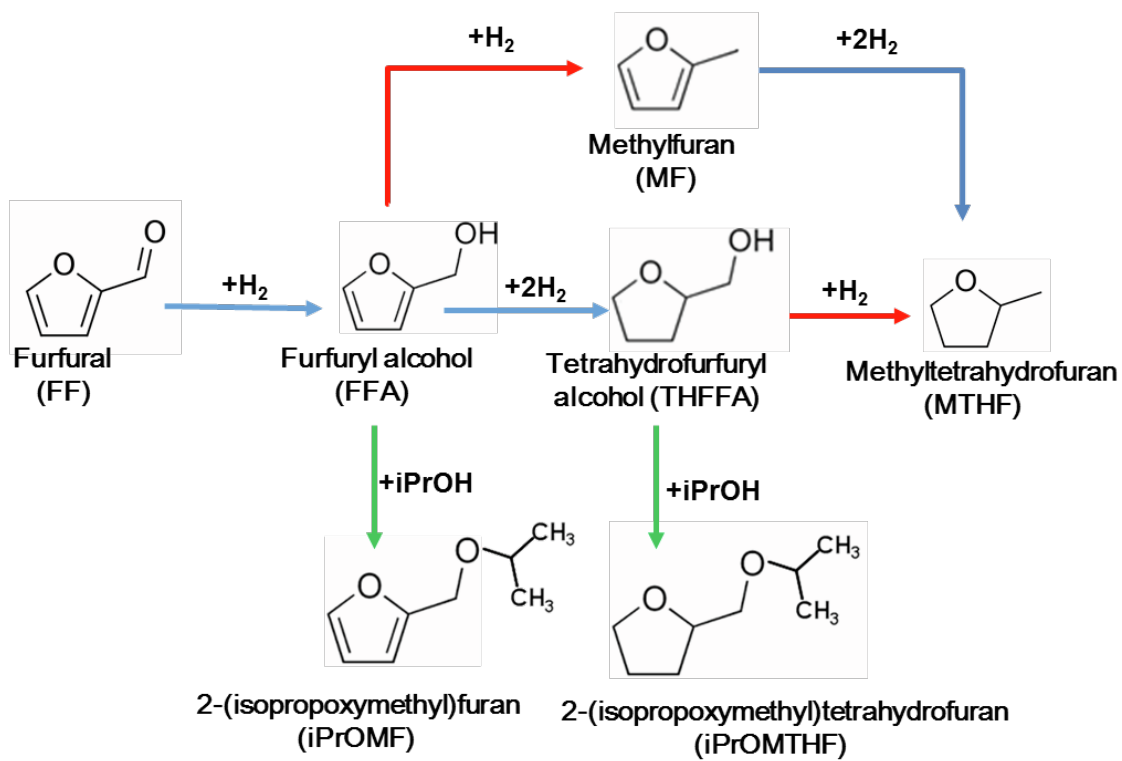
Figure S9. Reactions between furfural, its derivatives and H_2. Blue arrows: hydrogenation; red arrows, hydrogenolysis; green arrows: etherification with isopropanol.

Table S10. Carbon balance as a function of (time * mass). Carbon balances are calculated by summing the amounts of remaining furfural and of produced molecules.

(time* mass)	Carbon balance (%)						
	$Ni_{35}Fe_{65}/$ SiO_2	$Ni_{55}Fe_{45}/$ SiO_2	$Ni_{62}Fe_{38}/$ SiO_2	$Ni_{73}Fe_{27}/$ SiO_2	$Ni_{84}Fe_{16}/$ SiO_2	$Ni_{92}Fe_8/$ SiO_2	$Ni_{100}/$ SiO_2
1.5	90	88	96	93	99	97	99
2.5	89	90	98	98	99	99	99
5	88	84	94	95	92	99	93
10	85	89	94	99	99	99	90
20	85	86	99	99	99	98	93
40	85	91	92	99	99	98	95

Reaction conditions: T = 150 °C, P(H$_2$) = 20 bar, solvent: isopropanol, volume of solution: 1.5 mL, m$_{catalyst}$ = 3 – 10 mg, t = 0.5 – 4 h.

Table S11. Selectivities of products obtained for Ni-Fe/SiO$_2$ and Ni/SiO$_2$ catalysts at full conversion, for a product (time * mass) = 20 h mg.

Catalysts	Selectivity (%)					
	FFA	iPrOMF	THFFA	iPrOMTHF	MF	MTHF
$Ni_{62}Fe_{38}/SiO_2$	82.3	7.4	3.8	0	6.5	0
$Ni_{73}Fe_{27}/SiO_2$	77.3	8.1	4.7	0	9.9	0
$Ni_{84}Fe_{16}/SiO_2$	33.6	34.7	7.3	0	20.3	4.1
$Ni_{92}Fe_8/SiO_2$	20.0	31.6	20.0	2.1	19.5	6.8
Ni_{100}/SiO_2	4.6	30.6	22.2	9.9	10.2	22.5

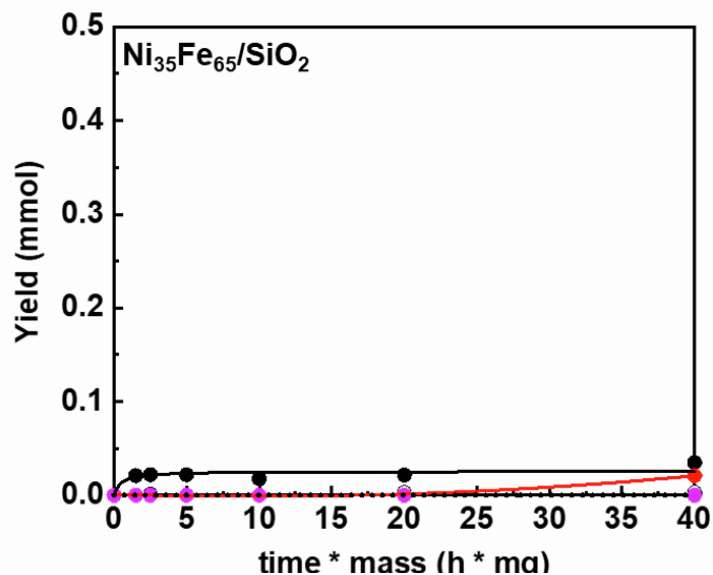Reaction conditions: T = 150 °C, P(H$_2$) = 20 bar, solvent: isopropanol, volume of solution: 1.5 mL.

Figure S10. Yield of products as a function of (time * mass) for Ni$_{35}$Fe$_{65}$/SiO$_2$ catalysts. Black line (●): FFA; Black dotted line (⊙): iPrOMF; Red line (●): MF; Purple line (●): MTHF. Reaction conditions: T = 150 °C, P(H$_2$) = 20 bar, solvent: isopropanol, volume of solution: 1.5 mL, m$_{catalyst}$ = 3 – 10 mg, t = 0.5 – 4 h.
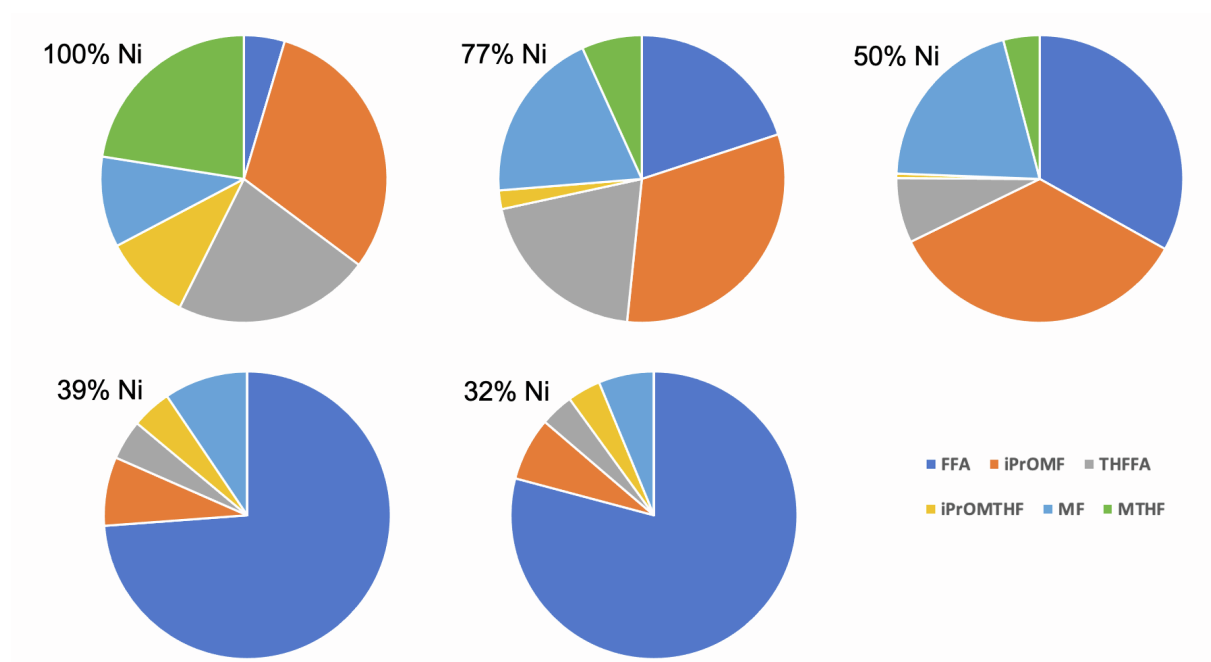

Figure S11. Selectivity chart representing the relationship between the surface nickel proportion determined by LEIS (measured at a cumulative iso-dose of 4.1 x 1015 Ne+ ions.cm^{-2}, Figure 4) and products distribution (Reaction conditions: T = 150 °C, P(H$_2$) = 20 bar, solvent: isopropanol, volume of solution: 1.5 mL, m$_{catalyst}$ = 10 mg, t = 4 h)

Table S12. Catalytic performance of catalysts $Ni_{62}Fe_{38}/SiO_2$ and Ni_{100}/SiO_2 for three successive catalytic runs.

Catalyst		Conversion (%)	Carbon balance (%)	Selectivity (%)				
				FFA	iPrOMF	THFFA	MF	MTHF
$Ni_{62}Fe_{38}/Si$	Run 1	83	94	86.0	10.6	0.7	2.7	0
O_2	Run 2	96	96	91.7	4.8	0.8	2.7	0
(t = 65 min)	Run 3	85	95	94.0	3.6	1.0	1.4	0
$Ni_{100}/$	Run 1	82	96	42.7	35.8	4.3	11.1	0.4
SiO_2	Run 2	84	97	62.9	23.4	3.1	7.0	0.3
(t = 35 min)	Run 3	72	99	69.5	23.5	2.2	4.1	0

Reaction conditions: T = 150 °C, P(H$_2$) = 20 bar, solvent: isopropanol, $C_{0(Furfural)}$ = 0.38 mol L^{-1}, volume of solution: 24 mL, $m_{catalyst}$ = 174 mg.
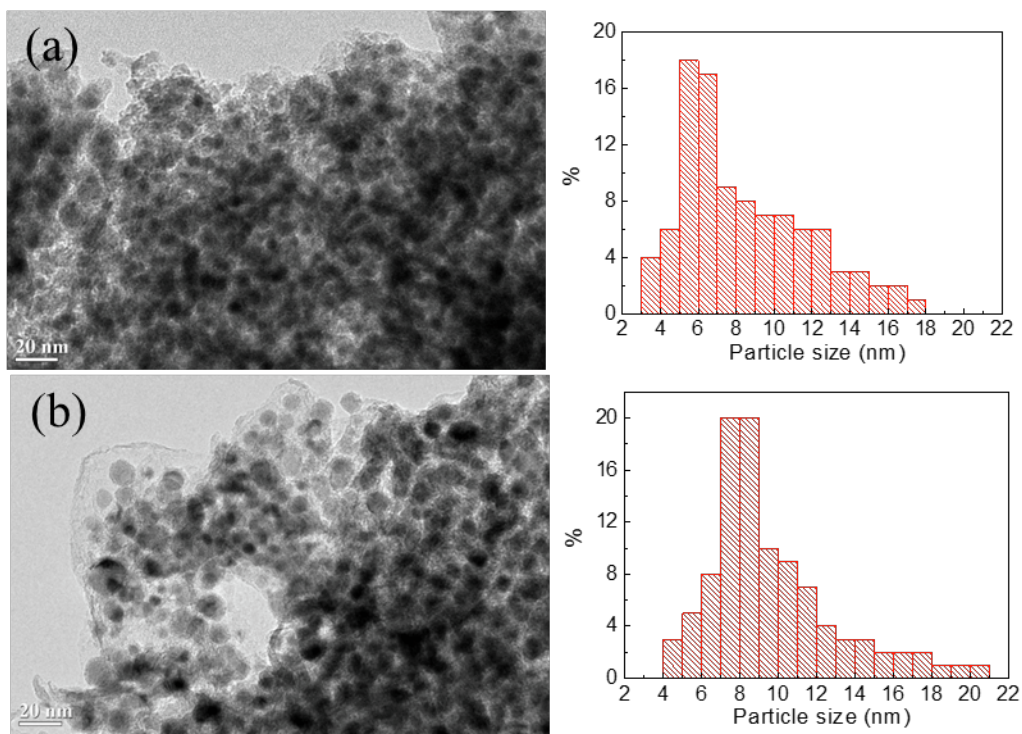
Figure S12. Bright field TEM micrographs and particle size distributions measured by TEM for $Ni_{62}Fe_{38}/SiO_2$ (a) and Ni_{100}/SiO_2 (b) catalysts after three runs of reaction and exposure to air.
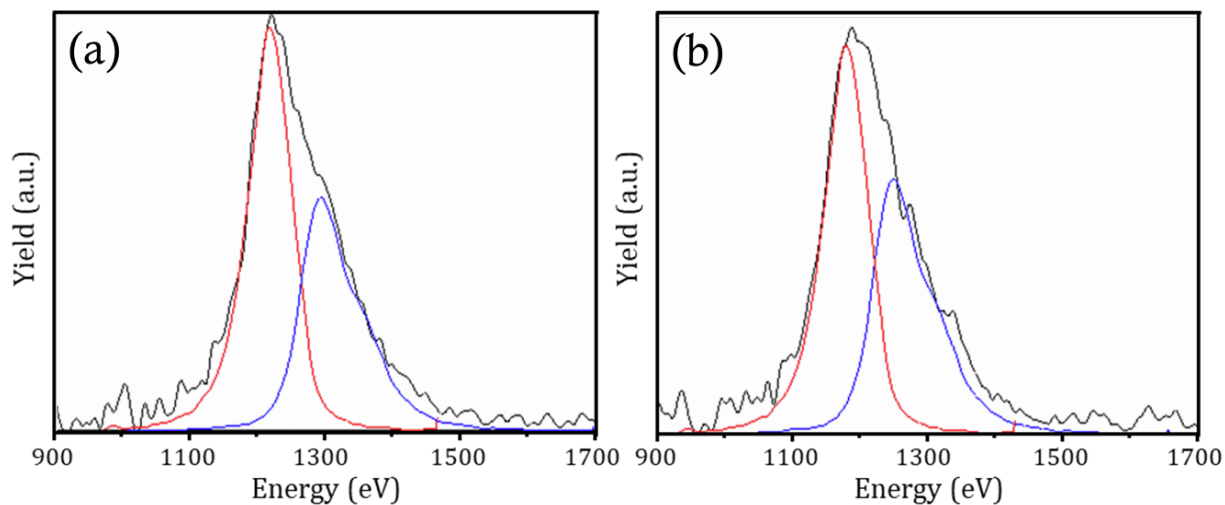

Figure S13. LEIS signal recorded for a dose of 4.1×10^{15} Ne^+ ions cm^{-2} for pristine $Ni_{62}Fe_{38}/SiO_2$ (a) and the same catalyst after three runs of reaction (b) (catalysts were re-activated in H_2 at 400 °C prior to analysis).
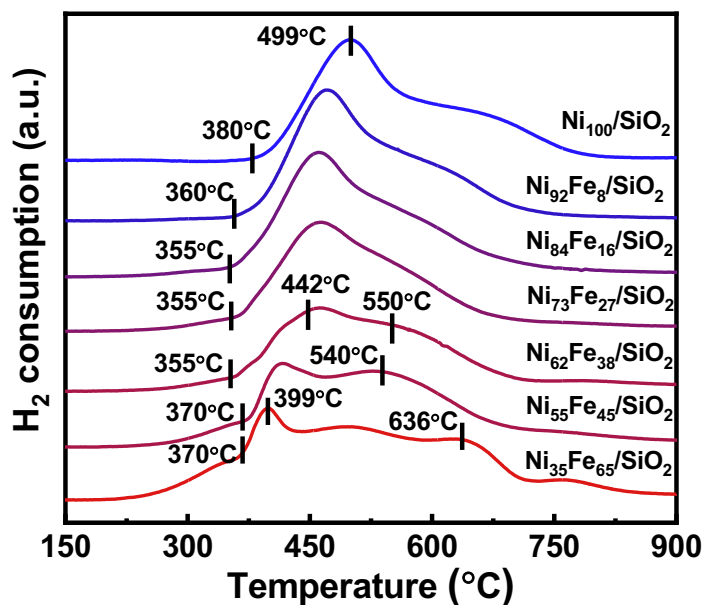

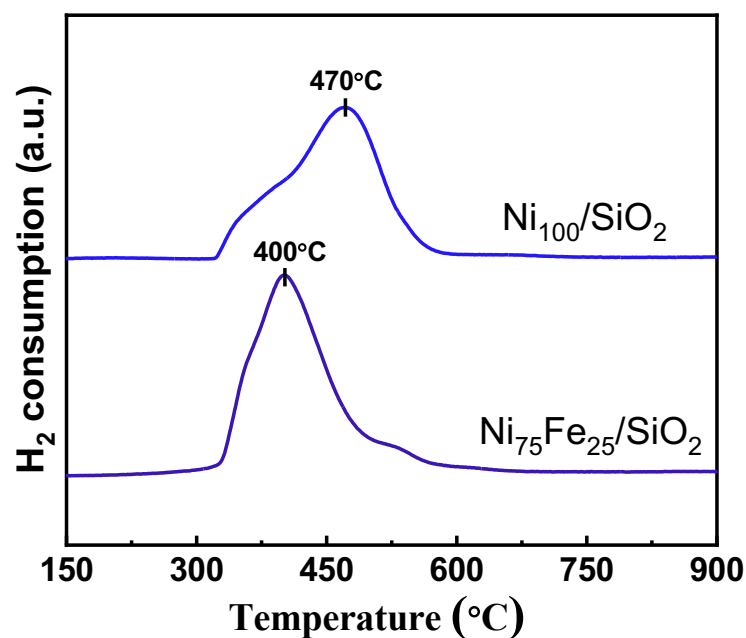**Figure S14.** Temperature-programmed reduction profiles of Ni-Fe/SiO$_2$ solids prepared by DPU and dried at 60 °C.

Figure S15. Temperature-programmed reduction profiles of catalysts $Ni_{75}Fe_{25}/SiO_2$ and Ni_{100}/SiO_2 prepared by incipient wetness impregnation (see Table xx). The reduction of two catalysts is total at about 600 °C in the conditions of TPR (diluted H_2, kinetic control).

Table S13. Comparison of the catalytic performance of catalysts $Ni_{62}Fe_{38}/SiO_2$ and Ni_{100}/SiO_2 prepared by DPU, without initial reduction at 700 °C; and catalysts $Ni_{75}Fe_{25}/SiO_2$ and Ni_{100}/SiO_2 prepared by incipient wetness impregnation (IWI),[a] with or without initial reduction at 700 °C.

Catalyst	Conversion (%)	Carbon balance (%)	Yield (mmol)				
			FFA	iPrOMF	THFFA	MF	MTHF
$Ni_{62}Fe_{38}/SiO_2$ DPU no reduction at 700 °C m = 10 mg, t = 2 h	100	99	0.22	0.24	0.02	0.04	0.01
Ni_{100}/SiO_2 DPU no reduction at 700 °C m = 10 mg, t = 2 h	98	99	0.01	0.26	0.07 (iPrOMTHF: 0.02)	0.12	0.08
$Ni_{75}Fe_{25}/SiO_2$ IWI no reduction at 700 °C m = 30 mg, t = 2 h	96	91	0.45	0.01	0.03	0.01	0
$Ni_{75}Fe_{25}/SiO_2$ IWI reduction at 700 °C m = 30 mg, t = 4 h	95	93	0.44	0.01	0.03	0.02	0

| Ni$_{100}$/SiO$_2$ IWI no reduction at 700 °C m = 30 mg, t = 2 h | 82 | 90 | 0.31 | 0.01 | 0.04 | 0.01 | 0 |
| Ni$_{100}$/SiO$_2$ IWI reduction at 700 °C m = 30 mg, t = 4 h | 95 | 91 | 0.39 | 0.01 | 0.07 | 0.02 | 0 |

Temperature of activation in H$_2$ = 400 °C. Reaction conditions: T = 150 °C, P(H$_2$) = 20 bar, solvent: isopropanol, volume of solution: 1.5 mL. [a.] The two control IWI catalysts (total loading in metals: 20 wt%) were prepared by incipient wetness impregnation of silica Sipernat-50, using Fe(NO$_3$)$_3$. 9 H$_2$O and/or Ni(NO$_3$)$_2$. 6H$_2$O as precursors. Loadings and Ni/Fe proportions were verified by XRF. The impregnated support was dried overnight at 60 °C under static air and further calcined for 10 h at 500 °C in a muffle oven. The IWI catalysts were either reduced at 700 °C following the protocol given for the DPU catalysts and re-activated in H$_2$ at 400 °C prior to catalytic reaction, or only activated in H$_2$ at 400 °C prior to catalytic reaction. The mass of catalyst and the reaction time were adjusted to obtain similar conversions.

Table S14. [57]Fe Mössbauer hyperfine parameters of samples Ni$_{35}$Fe$_{65}$/SiO$_2$, Ni$_{55}$Fe$_{45}$/SiO$_2$, Ni$_{62}$Fe$_{38}$/SiO$_2$, Ni$_{73}$Fe$_{27}$/SiO$_2$ and Ni$_{84}$Fe$_{16}$/SiO$_2$ after drying (see **Figure S16**). Spectra were recorded at room temperature.

Samples	Site	δ (mm s^{-1})	Δ (mm s^{-1})	Γ (mm s^{-1})	Area (%)	Average Δ (mm s^{-1})
Ni$_{35}$Fe$_{65}$/SiO$_2$	Fe(III) Oh	0.37± 0.01	1.25 ± 0.03	0.48 ± 0.01	33 ± 3	0.93
	Fe(III) Oh	0.35± 0.01	0.78 ± 0.02	0.48 ± 0.01	67 ± 3	
Ni$_{55}$Fe$_{45}$/SiO$_2$	Fe(III) Oh	0.35 ± 0.01	1.10 ± 0.02	0.40 ± 0.02	42 ± 2	0.82
	Fe(III) Oh	0.33 ± 0.01	0.62 ± 0.02	0.40 ± 0.02	58 ± 2	
Ni$_{62}$Fe$_{38}$/SiO$_2$	Fe(III) Oh	0.36 ± 0.01	1.12 ± 0.04	0.44 ± 0.02	36 ± 4	0.80
	Fe(III) Oh	0.33 ± 0.01	0.62 ± 0.02	0.44 ± 0.02	64 ± 4	
Ni$_{73}$Fe$_{27}$/SiO$_2$	Fe(III) Oh	0.37 ± 0.03	1.18 ± 0.09	0.43 ± 0.03	21 ± 6	0.75
	Fe(III) Oh	0.33 ± 0.01	0.63 ± 0.03	0.43 ± 0.03	79 ± 6	
Ni$_{84}$Fe$_{16}$/SiO$_2$	Fe(III) Oh	0.34 ± 0.01	1.05 ± 0.03	0.36 ± 0.02	36 ± 3	0.71
	Fe(III) Oh	0.31 ± 0.01	0.52 ± 0.02	0.36 ± 0.02	64 ± 4	

δ: isomer shift; Δ: electric quadrupole splitting; Γ: line width at half maximum.
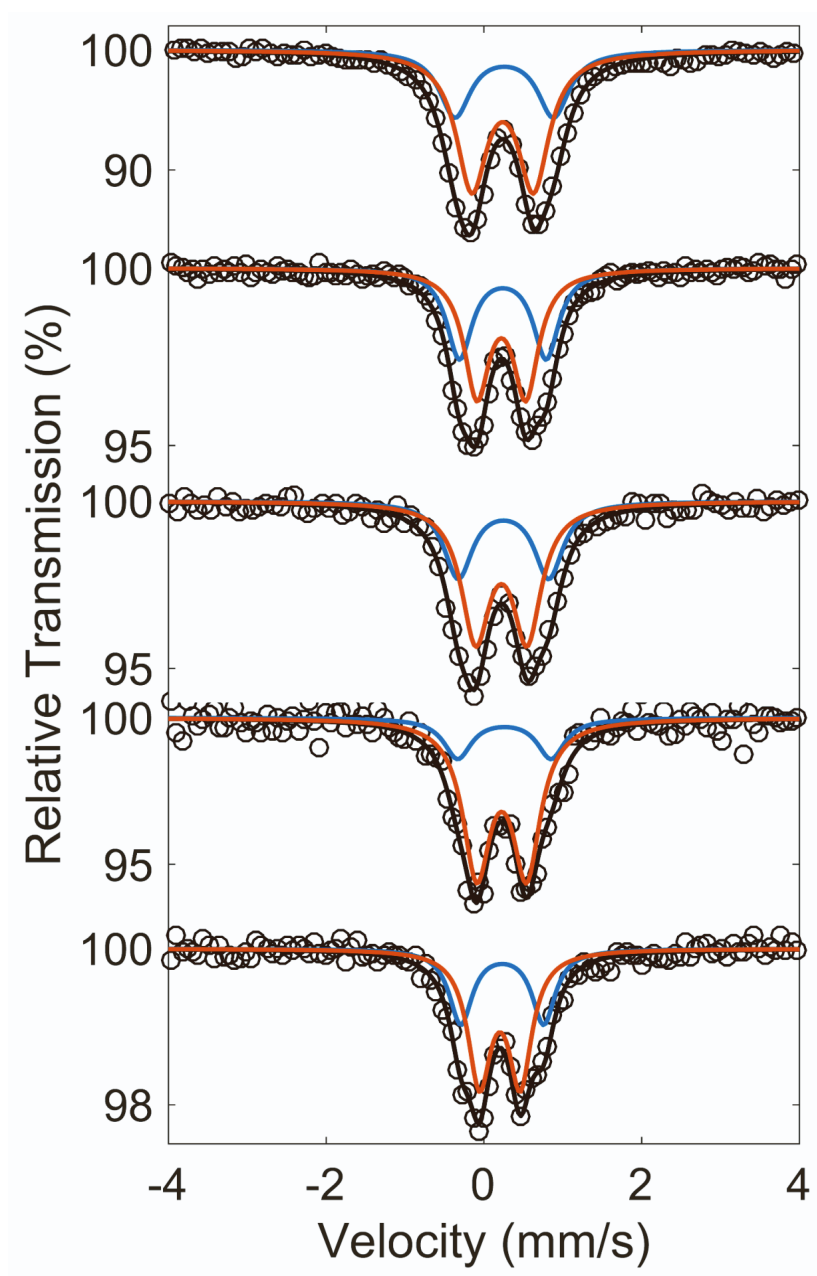
Figure S16. ^{57}Fe Mössbauer spectra of dried samples $Ni_{35}Fe_{65}/SiO_2$, $Ni_{55}Fe_{45}/SiO_2$, $Ni_{62}Fe_{38}/SiO_2$, $Ni_{73}Fe_{27}/SiO_2$ and $Ni_{84}Fe_{16}/SiO_2$ (from top to bottom). Spectra were recorded at room temperature.

REFERENCES

(1)   Li, H.; Zhang, S.; Luo, H. (2004), A Ce-promoted Ni–B amorphous alloy catalyst (Ni–Ce–B) for liquid-phase furfural hydrogenation to furfural alcohol. Mater Lett, *58*, 2741-2746

(2)   Li, H.; Luo, H.; Zhuang, L.; Dai, W.; Qiao, M. (2003), Liquid phase hydrogenation of furfural to furfuryl alcohol over the Fe-promoted NiB amorphous alloy catalysts. J Mol Catal A, *203*, 267-275

(3)   Xu, C.H.; Zheng, L.K.; Liu, J.Y.; Huang, Z.Y. (2011), Furfural hydrogenation on nickel-promoted Cu-containing catalysts prepared from hydrotalcite-like precursors. Chin J Chem, *29*, 691-697

(4)   Wei, S.Q.; Cui, H.Y.; Wang, J.H., Zhuo, S.P., Li, W.M.; Wang, L.H. et al. (2011), Preparation and activity evaluation of NiMoB/γ-Al₂O₃ catalyst by liquid-phase furfural hydrogenation. Particuology, *9*, 69-74

(5)   Lee, S.P.; Chen, Y.W.; (1999) Selective hydrogenation of furfural on Ni−P, Ni−B, and Ni−P−B ultrafine materials. Ind Eng Chem Res, *38*, 2548-2556

(6)   Vetere,V.; Merlo, A.B.; Ruggera, J.F.; Casella, M.L. (2010), Transition metal-based bimetallic catalysts for the chemoselective hydrogenation of furfuraldehyde. J Braz Chem Soc, 21, 914-920

(7)   Yan, K.; Chen, A.C. (2013), Efficient hydrogenation of biomass-derived furfural and levulinic acid on the facilely synthesized noble-metal-free Cu–Cr catalyst. Energy, 58, 357-363

(8)   Chen, X.; Li,H.; Luo, H.; Qiao, M. (2002). Liquid phase hydrogenation of furfural to furfuryl alcohol over Mo-doped Co–B amorphous alloy catalysts. Appl Catal A, *233*, 13-20

(9)   Khairi, S.; Rodiansono, T.; Hara, N.; Ichikuni, S.; Shimazu**.** (2012). Highly efficient and selective hydrogenation of unsaturated carbonyl compounds using Ni–Sn alloy catalysts**.** Catal Sci Technol, 2, 2139-2145

(10)   Sitthisa, S.; An, W.; Resasco, D. E.; (2011). Selective conversion of furfural to methylfuran over silica-supported NiFe bimetallic catalysts, Journal of Catalysis, *284*, 90-101.

(11)   Chieffi, G.; Giordano, C.; Antonietti, M.; Esposito, D. (2014), FeNi nanoparticles with carbon armor as sustainable hydrogenation catalysts: towards biorefineries, Journal of Materials Chemistry A, 2, 11591.

(12)   Putro, W. S.; Kojima, T.; Hara, T.; Ichikuni, N.; Shimazu, S., (2017). Selective hydrogenation of unsaturated carbonyls by Ni-Fe-based alloy catalysts, Catalysis Science & Technology, 7, 3637-3646.

(13)   Halilu, A.; Ali, T. H.; Atta, A. Y.; Sudarsanam, P.; Bhargava, S.K.; Abd Hamid, S.B. (2016), Highly selective hydrogenation of biomass-derived furfural into furfuryl alcohol using a novel magnetic nanoparticles catalyst, Energy & Fuels, 30, 2216-2226

(14)   Shi, D.; Yang, Q.; Peterson, C.; Lamic-Humblot, A. F.; Girardon, J. S.; Griboval-Constant, A.; Stievano, L.; Sougrati, M. T.; Briois, V.; Bagot, P. A. J.; Wojcieszak, R.; Paul, S.; Marceau, E. (2019). Bimetallic Fe-Ni/SiO₂ Catalysts for Furfural Hydrogenation: Identification of the Interplay between Fe and Ni during Deposition-Precipitation and Thermal Treatments. Catal. Today *334*, 162–172. 10.1016/j.cattod.2018.11.041.

(15)   Sadier, A.; Shi, D.; Mamede, A. S.; Paul, S.; Marceau, E.; Wojcieszak, R. (2021). Selective Aqueous Phase Hydrogenation of Xylose to Xylitol over SiO₂-Supported Ni and Ni-Fe Catalysts: Benefits of Promotion by Fe. Appl. Catal. B Environ. *298*, 120564. 10.1016/j.apcatb.2021.120564.